

# Antiperovskite Ionic Conductor Layer for Stabilizing the Interface of NASICON Solid Electrolyte Against Li Metal in All-Solid-State Batteries\*\*

Lei Gao,<sup>[a, b, c]</sup> Ruo Zhao,<sup>[b]</sup> Songbai Han,\*<sup>[b]</sup> Shuai Li,\*<sup>[b]</sup> Ruqiang Zou,\*<sup>[a, c]</sup> and Yusheng Zhao\*<sup>[b]</sup>

The instability of the interface between solid-state electrolytes (SSEs) and Li metal anodes is a critical factor restricting the application of NASICON-type ionic conductors in all-solid-state lithium batteries (ASSLBs). Here, the lithium-rich antiperovskite (LiRAP)  $\text{Li}_2\text{OHBr}$  ionic conductor is introduced as a protective layer for the NASICON-type solid electrolyte  $\text{Li}_{1.5}\text{Al}_{0.5}\text{Ge}_{1.5}(\text{PO}_4)_3$  (LAGP) by a simple way of rapid solidification of molten  $\text{Li}_2\text{OHBr}$ , to prevent the adverse reaction caused by direct contact

between LAGP and Li metal. The Li/Li symmetric cells with  $\text{Li}_2\text{OHBr}$  protective layer exhibit long-term cycle stability compared with the bare LAGP, and the mechanisms are analyzed by XPS measurements for the interface between SSEs and Li metal. Also, the  $\text{LiFePO}_4/\text{Li}$  ASSLBs have been assembled to further demonstrate this advantage. This work shows that LiRAP  $\text{Li}_2\text{OHBr}$  can improve the cycling stability of ASSLBs from the perspective of Li metal anode protection.

## 1. Introduction

Li-ion batteries (LIBs) have been widely applied in consumer electronics, electric vehicles, and stationary energy storage systems owing to their excellent electrochemical performances, and the demand for safer Li secondary batteries with higher energy density is still increasing simultaneously.<sup>[1]</sup> Whereas, the safety of current LIBs is challenged due to the flammability of the liquid electrolytes in thermal runaway behavior,<sup>[2]</sup> and the application of Li metal anode is limited in LIBs with liquid electrolytes due to the formation of dendrites,<sup>[3]</sup> which leads to the restriction on the increase in energy density.<sup>[4]</sup> To overcome these obstacles, inorganic solid-state electrolytes (SSEs) have been introduced into LIBs for their merits of nonflammability,<sup>[5]</sup> good electrochemical stability,<sup>[6]</sup> and applicability for the next generation of high-safety and high energy density all-solid-state lithium batteries (ASSLBs).<sup>[7]</sup> Consequently, a variety of

SSEs with high ionic conductivity have been discovered and investigated in recent years.<sup>[8]</sup>

Among these candidate SSEs, the NASICON-type ionic conductors ( $\text{Li}_{1+x}\text{Al}_x\text{M}_{2-x}(\text{PO}_4)_3$ , M=Zr, Ti, Ge, etc.) are considered to be one of the most promising SSEs for commercial ASSLBs, due to their high ionic conductivity, stability to air and moisture, and easiness for synthesis and sintering.<sup>[9]</sup> However, there is still a key challenge limiting the development of ASSLBs based on the NASICON-type SSEs, that is, the instability of interface between the NASICON-type SSEs and Li metal anode.<sup>[10]</sup> Representatively, recent studies on the chemical reaction between  $\text{Li}_{1.5}\text{Al}_{0.5}\text{Ge}_{1.5}(\text{PO}_4)_3$  (LAGP) and Li metal showed that the chemically formed interphase strongly affects the mechanical integrity of LAGP pellet.<sup>[11]</sup> Rapid capacity loss due to the formation of mixed conducting interphase at the LAGP/lithium interface has also been reported.<sup>[12]</sup> Besides, the morphological evolution of the interphase during cycling in symmetric Li/LAGP/Li cells is dependent on the current density, which has been proven by *in situ* transmission electron microscopy (TEM).<sup>[13]</sup> Therefore, stabilizing the Li/LAGP interface has become the prerequisite for LAGP to be used as a practical candidate SSE for all-solid-state Li metal batteries.<sup>[10b,14]</sup>

A variety of strategies have been proposed to improve the stability of the interface between the NASICON-type SSEs and Li metal. For example, polymer coatings were reported to improve electrochemical stability and compatibility of LAGP to Li metal.<sup>[12b,15]</sup> However, whether the polymer can prevent the penetration of Li dendrites has been the focus of debate among researchers. The  $\text{Al}_2\text{O}_3$ -coated LATP [ $\text{Li}_{1.3}\text{Al}_{0.3}\text{Ti}_{1.7}(\text{PO}_4)_3$ ] by atomic layer deposition (ALD) exhibited a stable cycling behavior and small resistance, which suggested that ALD is effective in improving SSE/electrode interface stability.<sup>[10c]</sup> Whereas, in fact,  $\text{Al}_2\text{O}_3$  is not an ionic conductor, which is unfavorable for Li-ions to shuttle between LATP and Li metal, and similar limitation exists in the recently reported work of Ge

[a] L. Gao, Prof. R. Zou  
Beijing Key Laboratory of Theory and Technology of Advanced Battery Material  
School of Materials Science and Engineering  
Peking University, Beijing 100871, China  
E-mail: rzou@pku.edu.cn

[b] L. Gao, Dr. R. Zhao, Prof. S. Han, Prof. S. Li, Prof. Y. Zhao  
Academy for Advanced Interdisciplinary Studies and Department of Physics  
Shenzhen Key Laboratory of Solid State Batteries  
Guangdong Provincial Key Laboratory of Energy Materials for Electric Power  
Southern University of Science and Technology  
Shenzhen 518055, China  
E-mail: hansb@sustech.edu.cn  
lis6@sustech.edu.cn  
zhaoy@sustech.edu.cn

[c] L. Gao, Prof. R. Zou  
Institute of Clean Energy  
Peking University, Beijing 100871, China

[\*\*] NASICON: Sodium (Na) Super Ionic CONductor

Supporting information for this article is available on the WWW under  
<https://doi.org/10.1002/batt.202100123>

metal coating on LAGP.<sup>[11c]</sup> Also, the amorphous LAGP layer was formed on the ceramic LAGP via a spin-coating co-sintering method to insulate the internal electrolyte from the external highly reducing environment,<sup>[14a]</sup> but the existence of Ge<sup>4+</sup> in the amorphous LAGP layer may lead to the inevitable reduction reaction. To address these challenges, we propose to use lithium-rich antiperovskite (LiRAP)<sup>[16]</sup> Li<sub>2</sub>OHBr ionic conductor as a protective layer to prevent the adverse reaction caused by direct contact between LAGP and Li metal,<sup>[11c,17]</sup> and the reason that LiRAP Li<sub>2</sub>OHBr is specifically chosen in this work is as follows. Firstly, the LiRAP family has been proven to be stable to metallic lithium in symmetric Li/LiRAP/Li cells<sup>[18]</sup> and ASSLBs.<sup>[19]</sup> In this case, the interface between LiRAP and Li metal would be stable during cycling. Secondly, Li<sub>2</sub>OHBr possesses high ionic conductivity ( $>10^{-6}$  S/cm) at room temperature (RT),<sup>[19–20]</sup> which could support the fast shuttle of lithium ions between LAGP and Li metal. Thirdly, since the melting point of Li<sub>2</sub>OHBr is only  $\sim 254^{\circ}\text{C}$ ,<sup>[21]</sup> it is easy for the direct solidification of molten Li<sub>2</sub>OHBr into desired shape and forming a protective layer on LAGP,<sup>[18,20,22]</sup> and does not need a special customized mold to provide mechanical pressure to avoid imperfect physical contact between SSEs and protective layer.<sup>[23]</sup> Fourthly, the mechanical property and flame retardancy of inorganic Li<sub>2</sub>OHBr are better than those of polymer composite solid electrolyte membranes,<sup>[12b,15,24]</sup> and it could protect LAGP from Li anode more effectively in ASSLBs.

Herein, the protective layer on the surface of LAGP pellet was formed by a simple way of rapid solidification of molten Li<sub>2</sub>OHBr, and the dense and smooth Li<sub>2</sub>OHBr layer was observed with scanning electron microscopy (SEM). The Li/Li symmetric

cells with Li<sub>2</sub>OHBr protective layer exhibit long-term cycle stability, compared with those using bare LAGP. XPS analysis was conducted to reveal the possible reasons for the stability of the interface between Li<sub>2</sub>OHBr-protected LAGP and Li metal. Besides, LiFePO<sub>4</sub>/SSEs/Li ASSLBs with protective layer of Li<sub>2</sub>OHBr were also assembled and showed good cycle and rate performances.

## 2. Results and Discussion

### 2.1. Characterizations of SSEs

The XRD pattern of LAGP powder and sintered LAGP pellet at room temperature are shown in Figure 1a. All the main peaks in the XRD pattern match well with the NASICON-type structure of LiGe<sub>2</sub>(PO<sub>4</sub>)<sub>3</sub> (LAGP, PDF#80-1922, R̄3c (167) space group), and details of the crystal can be obtained from previous work.<sup>[25]</sup> Due to the annealing at 950 °C for 10 h, the crystallinity of LAGP pellet becomes better after sintering, and thus exhibits a sharper peak shape than LAGP powder. The XRD patterns of Li<sub>2</sub>OHBr powder and layer on the LAGP pellet are shown in Figure 1b. The XRD pattern of Li<sub>2</sub>OHBr powder exhibits single-phase characteristics and matches well with the standard PDF card (#84-0101, Pm̄3m (221) space group), except for the bulge at the low angle, which is caused by the Kapton film. The OH<sup>-</sup> ions are coordinated by Li<sup>+</sup> ions, forming  $\langle \text{Li}_6\text{OH} \rangle$  octahedra with one-third of the Li vacancies for charge balance, and the Br<sup>-</sup> ions are located at the 12-fold coordinated cavity of the octahedral network. Interestingly, the Li<sub>2</sub>OHBr layer solidified

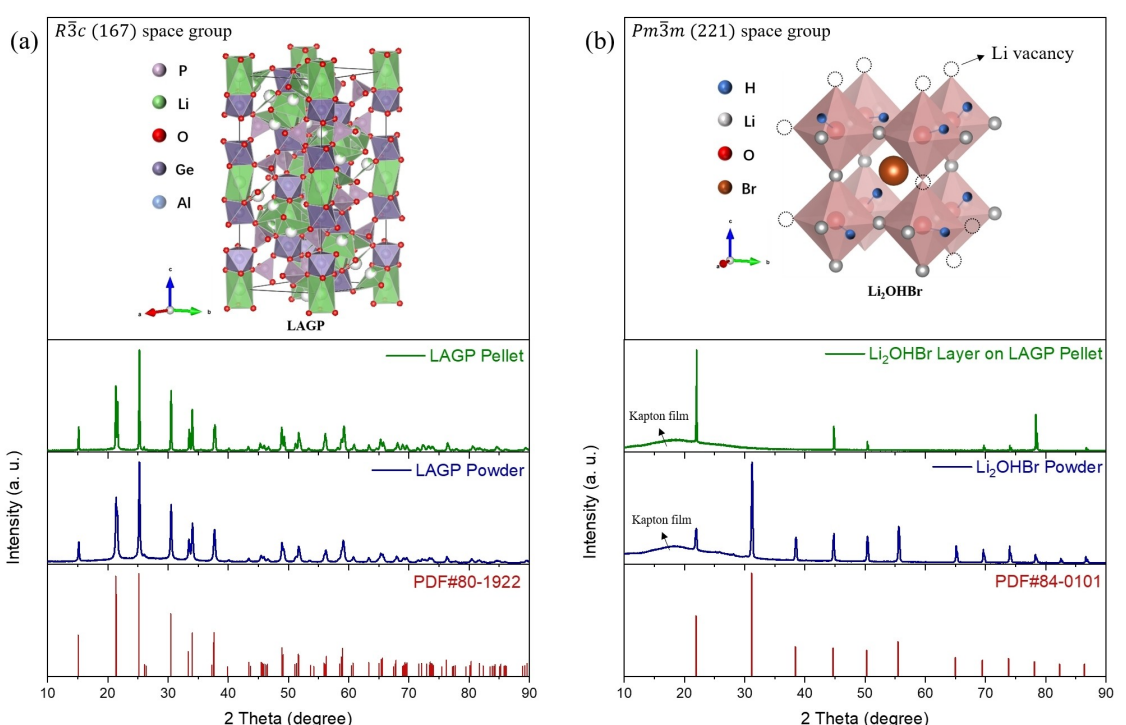


Figure 1. The schematic crystal structures and XRD patterns of a) LAGP and b) Li<sub>2</sub>OHBr.

on the surface of LAGP after melting and rapid cooling shows obvious orientation (e.g. the Miller index (100) direction), which has also been observed in our other experiments involving the rapid cooling of molten Li<sub>2</sub>OHBr. This orientation issue will be studied more systematically in our future works.

Before the preparation of Li<sub>2</sub>OHBr-protected LAGP pellets, the melting temperature of Li<sub>2</sub>OHBr was determined by DSC measurement. As shown in Figure 2S, the endothermic and exothermic peaks represent the melting and crystallization temperature of Li<sub>2</sub>OHBr, respectively. The melting point of Li<sub>2</sub>OHBr is about 257 °C, which is higher than the reported value of 254 °C,<sup>[21]</sup> and the slight difference in melting points may be related to the different synthesis conditions of the samples. The reported Li<sub>2</sub>OHBr was synthesized by ball milling at room temperature, which may help reduce the crystallinity of the samples and lead to a lower melting point.<sup>[26]</sup>

Figure 2a and Figure 2b show the Nyquist plots of Li<sub>2</sub>OHBr and LAGP measured in the temperature range between 25 and 100 °C, respectively. Taking the Nyquist curve of LAGP at 30 °C as a representative, as shown in Figure 2e, it exhibits a typical semicircle at high frequency representing the bulk and grain boundary resistance in series, and the linear part at low frequency representing ion blocking electrode. Fitting the Nyquist curve by the equivalent circuit leads to a total resistance  $R$  of 484 Ω, including the bulk resistance  $R_b$  of 200 Ω and the grain boundary resistance  $R_{gb}$  of 284 Ω. Further, we calculate the ionic conductivity is  $2.1 \times 10^{-4}$  S/cm based on the formula of  $\sigma = L/(RS)$ , where  $L$  (~1.2 mm),  $R$  (~484 Ω),  $S$  (~1.13 cm<sup>2</sup>) are the thickness, total resistance and area of LAGP pellet, respectively. Figure 2c and Figure 2d are the Arrhenius plots of Li<sub>2</sub>OHBr and LAGP illustrating the relationship between ionic conductivity and temperature in the range between 25

and 100 °C, and the ionic conductivities of Li<sub>2</sub>OHBr and LAGP are  $1.03 \times 10^{-6}$  S/cm and  $1.7 \times 10^{-4}$  S/cm at RT (25 °C), respectively. The activation energies  $E_a$  of Li<sub>2</sub>OHBr and LAGP are 0.597 eV and 0.360 eV respectively, which are fitted according to the slope of the plots following the Arrhenius law:  $\sigma = A \exp(-E_a/k_B T)$ . In which  $\sigma$  is the conductivity,  $A$  is the preexponential parameter,  $E_a$  is the activation energy,  $T$  is absolute temperature, and  $k_B$  is the Boltzmann constant. In addition, the Nyquist curve of the Li<sub>2</sub>OHBr-protected LAGP electrolyte at RT (25 °C) is shown in Figure 2f, which is fitted by the equivalent circuit leads to a total resistance  $R$  of 8.24 kΩ, including the bulk resistance  $R_b$  of 1.2 kΩ, the grain boundary resistance  $R_{gb}$  of 5.52 kΩ, and the interface resistance  $R_i$  of 1.52 kΩ. Further, the ionic conductivity is calculated to be  $1.4 \times 10^{-5}$  S/cm based on the formula of  $\sigma = L/(RS)$ , where  $L$  (~1.3 mm),  $R$  (~8.24 kΩ),  $S$  (~1.13 cm<sup>2</sup>) are the thickness, total resistance and area of the composite electrolyte, respectively.

Figure 3a shows the surface morphology of the sintered bare LAGP pellet, and Figure 3b shows the Li<sub>2</sub>OHBr protective layer on LAGP surface observed by SEM. For the LAGP pellet, distinct graininess could be observed, even after sintering and densification at 950 °C for 10 h. In contrast, the Li<sub>2</sub>OHBr protective layer on the surface of LAGP presents a smooth and dense morphology after Li<sub>2</sub>OHBr melting, rapid cooling, and solidification. These features may be beneficial to the uniformity of the current density during lithium ions intercalation/deintercalation and prevent lithium dendrite from penetrating the LAGP pellet through the pores and causing a short-circuit of the batteries. Figure 3c shows the cross-sectional morphology of the Li<sub>2</sub>OHBr-protected LAGP pellet, and the thickness of Li<sub>2</sub>OHBr layer is about 20 μm. Meanwhile, good adhesion can be observed in the transition region between LAGP pellet and

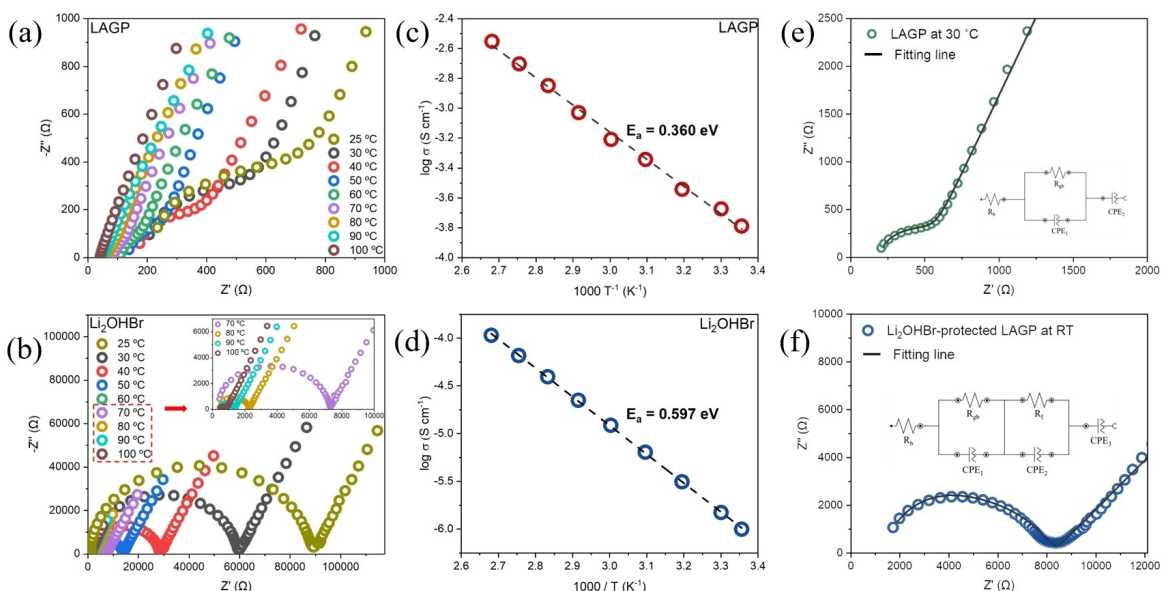


**Figure 2.** a), b) Nyquist plots of Li<sub>2</sub>OHBr and LAGP measured in the temperature range from 25 to 100 °C. c), d) The Arrhenius plots of Li<sub>2</sub>OHBr and LAGP illustrating the relationship between ionic conductivity and temperature in the range from 25 to 100 °C. e) Fitting curve with the equivalent circuit for Nyquist plot of LAGP at 30 °C. f) Fitting curve with the equivalent circuit for Nyquist plot of Li<sub>2</sub>OHBr-protected LAGP at RT (25 °C).

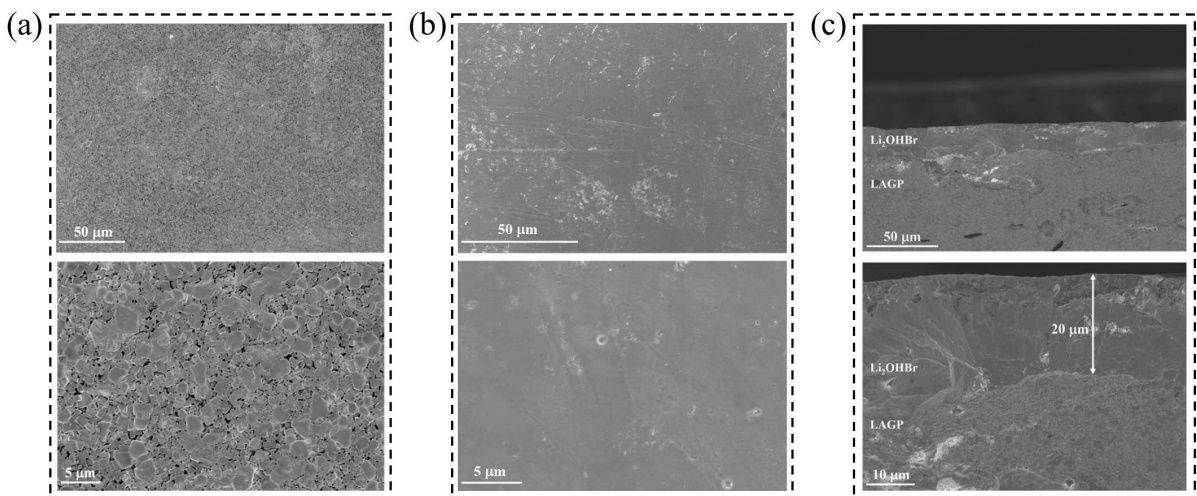


**Figure 3.** a) Surface morphology of the sintered bare LAGP pellet. b) Surface morphology of Li<sub>2</sub>OHBr protective layer on LAGP pellet. c) Cross-sectional morphology of the Li<sub>2</sub>OHBr-protected LAGP pellet, and the thickness of Li<sub>2</sub>OHBr layer is about 20 μm.

Li<sub>2</sub>OHBr layer, which may be due to the fact that molten Li<sub>2</sub>OHBr infiltrated into the pores of LAGP pellet.

## 2.2. Electrochemical Performance of Li/Li Symmetric Cells

Before the Li/Li symmetric cell tests, cyclic voltammetry (CV) measurement is conducted to investigate whether Li<sub>2</sub>OHBr

could prevent LAGP from being reduced with Li metal or not. In the CV tests, Li metal was used as the counter electrode and Au was used as the working electrode. As shown in Figure S3, the Li<sub>2</sub>OHBr-protected LAGP is highly stable in the range of -0.5–5.0 V versus Li/Li<sup>+</sup>, demonstrating no side reactions happen in the interphase.

The electrochemical performance of Li/Li symmetric cells is shown in Figure 4. With the galvanostatic cycling of Li/LAGP/Li

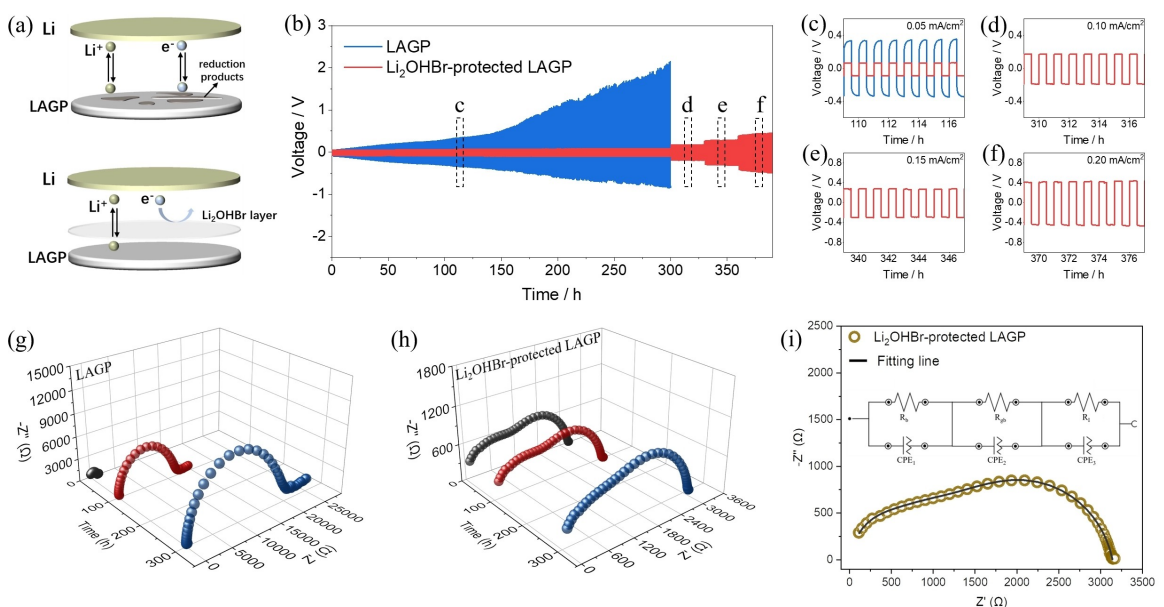


**Figure 4.** a) Schematic diagram of the evolution of the interface between LAGP and Li metal, direct contact of bare LAGP pellet with Li metal leads to the formation of reduction products (upper part), the interface between LAGP and Li metal is stabilized by the protection of Li<sub>2</sub>OHBr layer (lower part). b) Galvanostatic cycling of Li/LAGP/Li symmetric cell at current density of 0.05 mA/cm<sup>2</sup> (300 h) and Li/Li<sub>2</sub>OHBr/LAGP/Li<sub>2</sub>OHBr/Li symmetric cell at current density of 0.05 mA/cm<sup>2</sup> (300 h), 0.10 mA/cm<sup>2</sup> (30 h), 0.15 mA/cm<sup>2</sup> (30 h) and 0.20 mA/cm<sup>2</sup> (30 h). c), d), e), f) Insets of the specific period of the galvanostatic cycling. g), h) EIS of Li/LAGP/Li symmetric cell and Li/Li<sub>2</sub>OHBr/LAGP/Li<sub>2</sub>OHBr/Li symmetric cell at different cycle times. i) Fitting curve with the equivalent circuit for Nyquist plot of Li/Li symmetric cell of Li<sub>2</sub>OHBr-protected LAGP at 80 °C.

symmetric cell (Figure 4b), the obvious polarization was observed along with the increase of voltage at the current density of  $0.05 \text{ mA/cm}^2$ . In contrast, Li/Li<sub>2</sub>OHBr/LAGP/Li<sub>2</sub>OHBr/Li symmetric cell remained stable after a long-term galvanostatic cycling (Figure 4b-f;  $0.05 \text{ mA/cm}^2\text{-}300 \text{ h}$ ,  $0.10 \text{ mA/cm}^2\text{-}30 \text{ h}$ ,  $0.15 \text{ mA/cm}^2\text{-}30 \text{ h}$ , and  $0.20 \text{ mA/cm}^2\text{-}30 \text{ h}$ ). Meanwhile, the EIS plots of Li/Li symmetric cells (Figure 4g and 4 h) were analyzed to verify whether the Li<sub>2</sub>OHBr layer is beneficial to alleviate polarization. Taking the EIS plot of Li/Li<sub>2</sub>OHBr/LAGP/Li<sub>2</sub>OHBr/Li symmetric cell after 300 h cycle as a representative, as shown in Figure 4i, fitting it by the equivalent circuit leads to a total resistance  $R$  of  $3.14 \text{ k}\Omega$ , including the bulk resistance  $R_b$  of  $0.26 \text{ k}\Omega$ , the grain boundary resistance  $R_{gb}$  of  $1.76 \text{ k}\Omega$ , and the interface resistance  $R_i$  of  $1.12 \text{ k}\Omega$ . Before the galvanostatic cycling of the symmetric cells, the Li/Li<sub>2</sub>OHBr/LAGP/Li<sub>2</sub>OHBr/Li cell ( $2.63 \text{ k}\Omega$ ) shows a higher impedance than that of Li/LAGP/Li cell ( $1.46 \text{ k}\Omega$ ) due to the introduction of the Li<sub>2</sub>OHBr layer between LAGP and Li metal. However, with the galvanostatic cycling tests, the impedance of Li/LAGP/Li cell changed from  $1.46 \text{ k}\Omega$  to  $20.82 \text{ k}\Omega$  (after  $0.05 \text{ mA/cm}^2\text{-}300 \text{ h}$ ). Comparatively, Li/Li<sub>2</sub>OHBr/LAGP/Li<sub>2</sub>OHBr/Li cell only changed from  $2.63 \text{ k}\Omega$  to  $3.14 \text{ k}\Omega$  (after  $0.05 \text{ mA/cm}^2\text{-}300 \text{ h}$ ), which is due to the existence of Li<sub>2</sub>OHBr layer to stabilize the interface of LAGP against Li metal. Noteworthily, the resistance of  $2.63 \text{ k}\Omega$  is slightly high for Li/Li symmetric cell, which is unfavorable for operation at high current densities. The method of vacuum evaporation or spin-coating could be considered to reduce the thickness of Li<sub>2</sub>OHBr layer and the resistance of Li/Li cells in future experiments.

To further demonstrate the role of Li<sub>2</sub>OHBr layer in stabilizing LAGP against Li metal, we disassembled the Li/Li symmetric cells to observe the surface and cross-sectional morphology by SEM after galvanostatic cycling. For LAGP, as shown in Figure 5a (left), the morphology of surface deteriorated obviously, accompanied by surface cracks and reaction by-products (Figure 4S). In contrast, the surface morphology of Li<sub>2</sub>OHBr protective layer on LAGP still maintained flat (Figure 5a (right)), and there is no obvious difference from that before the Li/Li symmetric cell tests, except that the holes are found on the Li<sub>2</sub>OHBr layer, which may be caused by the continuous Li-ions shuttling between the Li metal and the Li<sub>2</sub>OHBr layer after a long galvanostatic cycling of Li/Li symmetric cell. Meanwhile, the good adhesion can still be observed in the transition region between Li<sub>2</sub>OHBr layer and Li metal, as well as the transition region between Li<sub>2</sub>OHBr layer and LAGP (Figure 5b), with correlating energy-dispersive X-ray spectroscopy (EDS) mapping of oxygen (existing in Li<sub>2</sub>OHBr, LAGP and Li metal) in green, bromine (existing in Li<sub>2</sub>OHBr) in orange, and germanium (existing in LAGP) in yellow. Noteworthily, the existence of oxygen in Li metal may be attributed to its susceptibility to oxidation.

Furthermore, the stability of the interface region was analyzed by XPS. For LAGP, as shown in Figure 5c, the binding energy of Ge<sup>4+</sup> for the 3d orbit is  $33.0 \text{ eV}$  and the binding energy corresponding to the Li 1s orbit is  $55.7 \text{ eV}$  before the galvanostatic cycling. After electrochemical cycles, in addition to the Ge<sup>4+</sup> peak, the peaks of Ge metal ( $29.5 \text{ eV}$ ) and Ge<sup>3+</sup> ( $31.2 \text{ eV}$ ) appeared in the Ge 3d data. Also, the Li 1s peak showed an obvious shift, which included the original peak of

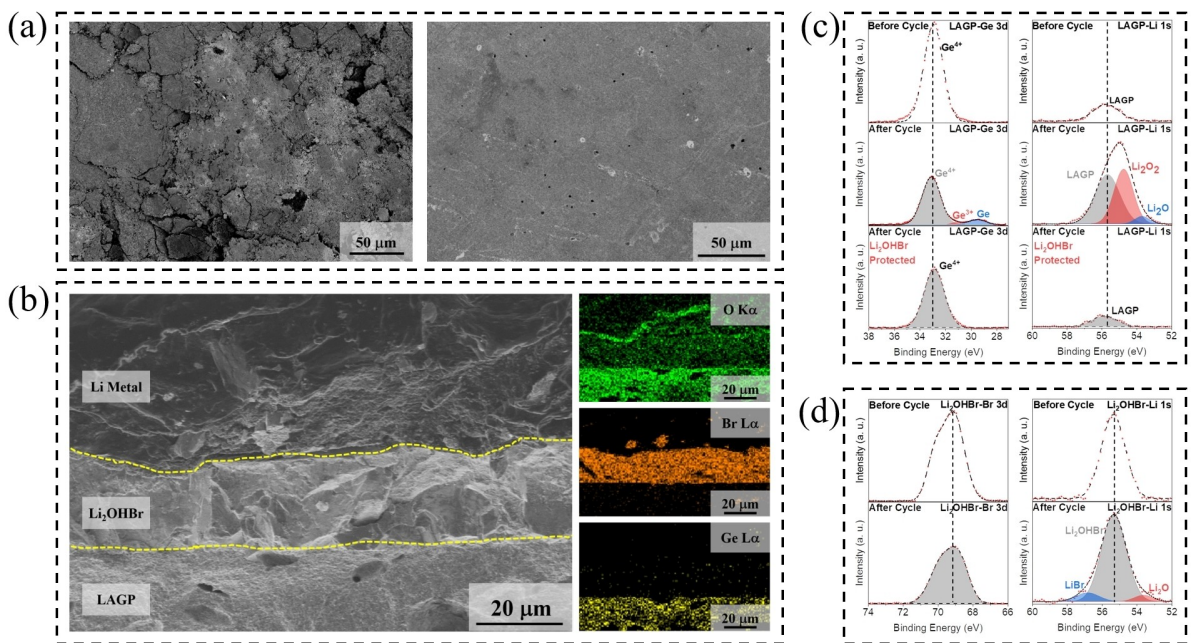
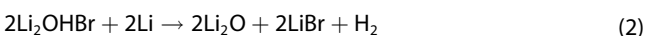
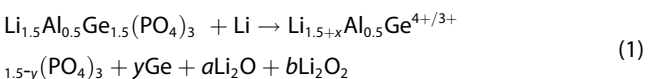


**Figure 5.** a) The morphology of LAGP surface (left) and Li<sub>2</sub>OHBr layer surface (right) after galvanostatic cycling of Li/Li symmetric cells. b) Cross-sectional morphology of the Li<sub>2</sub>OHBr-protected LAGP pellet after galvanostatic cycling of Li/Li symmetric cells, with correlating EDS mapping of oxygen in green, bromine in orange, and germanium in yellow. c) XPS of LAGP, data of Ge 3d and Li 1s before cycles (top), data of Ge 3d and Li 1s after cycles without Li<sub>2</sub>OHBr protecting (middle), data of Ge 3d and Li 1s after cycles with Li<sub>2</sub>OHBr protecting (bottom). d) XPS of Li<sub>2</sub>OHBr layers, data of Br 3d and Li 1s before cycles (top), data of Br 3d and Li 1s after cycles (bottom).

LAGP (55.7 eV), the peak of  $\text{Li}_2\text{O}_2$  (54.8 eV), and the peak of  $\text{Li}_2\text{O}$  (53.7 eV). These results indicated that LAGP was reduced by Li metal after cycling in Li/LAGP/Li cell, and the possible reaction mechanism [Equation (1)] is suggested. In particular, Ge metal, the decomposition product of LAGP, has electronic conductivity, which may lead to the continuous reactions between LAGP and Li metal, resulting in the increase of polarization and interface impedance of Li/LAGP/Li cells. Comparatively, the LAGP in Li/Li<sub>2</sub>OHBr/LAGP/Li<sub>2</sub>OHBr/Li cell did not show obvious changes after cycling, and the peaks of Ge 3d orbit and Li 1s orbit are consistent with those before cycling. For Li<sub>2</sub>OHBr layer, as shown in Figure 5d, the peaks of Br 3d and Li 1s after cycling remained similar to the main peaks before cycling, which indicates that Li<sub>2</sub>OHBr is stable to Li metal during cycling. This result is due to the excellent electronic insulation (as shown in Figure 5S,  $\sim 1.1 \times 10^{-8} \text{ S/cm}$  at 80 °C) and ionic conductivity of Li<sub>2</sub>OHBr. As a protective layer between LAGP and Li metal, Li<sub>2</sub>OHBr not only acts as an ion-transport layer but also prevents electron conduction between LAGP and Li metal, thereby effectively preventing the reaction between LAGP and Li metal (Figure 4a). Interestingly, in the XPS data of Li 1s, we noticed that there may be traces of LiBr and Li<sub>2</sub>O in Li<sub>2</sub>OHBr by fitting the spectra. This result is similar to that of Li<sub>2</sub>OHCl previously reported,<sup>[18]</sup> which infers Li<sub>2</sub>OHCl may react with Li metal to form LiCl and Li<sub>2</sub>O in the interface region during the high-temperature cycling at 195 °C, and this bulk solid electrolyte interphase (SEI, a mixture of LiCl and Li<sub>2</sub>O) forms an interconnected network that protects the Li<sub>2</sub>OHCl from further reacting with Li metal. Therefore, we speculate that a small amount of above-mentioned bulk SEI (a mixture of LiBr and Li<sub>2</sub>O) may be formed at the interface between Li<sub>2</sub>OHBr and Li metal during cycling of Li/Li<sub>2</sub>OHBr/LAGP/Li<sub>2</sub>OHBr/Li cell at 80 °C,

which prevents a further reaction between Li<sub>2</sub>OHBr and Li metal [as shown in Equation (2)].



### 2.3. Electrochemical Performance of LiFePO<sub>4</sub>/Li ASSLBs

After verifying that the Li<sub>2</sub>OHBr layer can be used to stabilize the interface of LAGP against the Li metal, LFP/SSEs/Li cells were assembled to further examine whether the Li<sub>2</sub>OHBr-protected LAGP electrolytes can be applied in all-solid-state batteries. As shown in Figure 6a, despite the LFP/Li ASSLB without Li<sub>2</sub>OHBr layer exhibits the initial specific capacity of 113.7 mAh g<sup>-1</sup>, it decays to less than 96 mAh g<sup>-1</sup> after 20<sup>th</sup> cycle at 0.1 C, only possessing poor capacity retention of 25.7 mAh g<sup>-1</sup> after 40<sup>th</sup> cycle. Such fast capacity decay is stimulated by the deteriorating LAGP/Li interface and rapidly increasing overpotential (Figure 6d). In contrast, the LFP/Li ASSLB with Li<sub>2</sub>OHBr layer exhibits the higher initial specific capacity of 119.9 mAh g<sup>-1</sup>, and remains the capacity of 110.1 mAh g<sup>-1</sup> after 20<sup>th</sup> cycle and the capacity of 96.3 mAh g<sup>-1</sup> after 40<sup>th</sup> cycle at 0.1 C, respectively (Figure 6b). Meanwhile, the increase in overpotential has been well alleviated compared to LFP/Li ASSLB without Li<sub>2</sub>OHBr layer (Figure 6e), which is due to the Li<sub>2</sub>OHBr layer effectively avoiding the reactions between LAGP and Li metal anode. Besides, rate performance was also

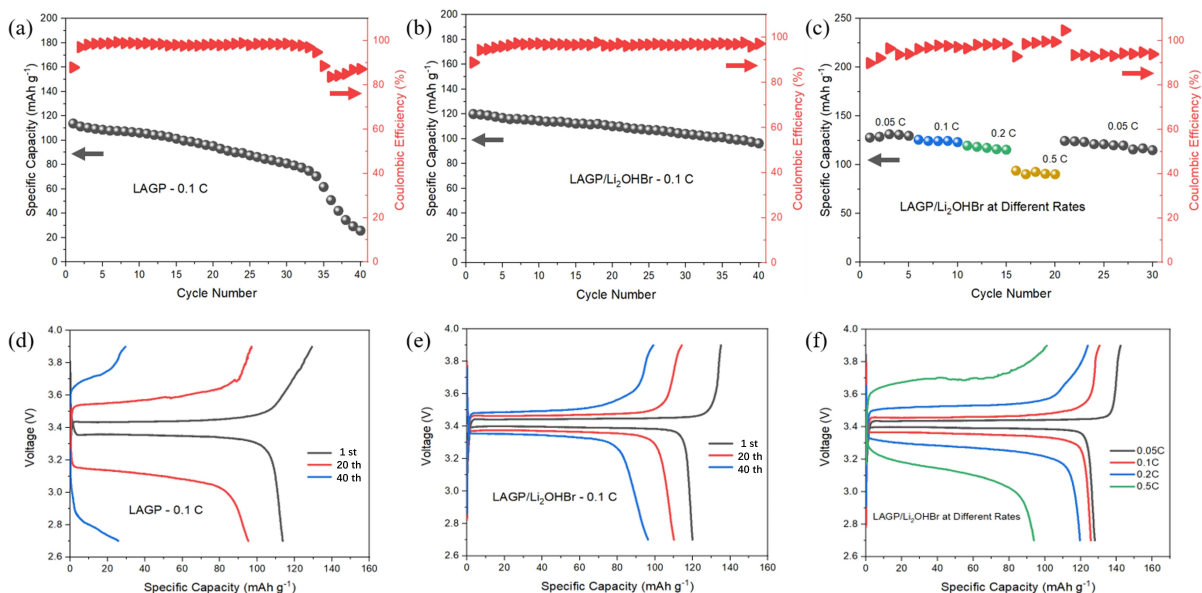


**Figure 6.** a) Cycling performance of LFP/Li ASSLB without Li<sub>2</sub>OHBr layer at 0.1 C. b) Cycling performance of LFP/Li ASSLB with Li<sub>2</sub>OHBr layer at 0.1 C. c) Cycling performance of LFP/Li ASSLB with Li<sub>2</sub>OHBr layer at different rates. d) Voltage profiles of LFP/Li ASSLB without Li<sub>2</sub>OHBr layer at 0.1 C. e) Voltage profiles of LFP/Li ASSLB with Li<sub>2</sub>OHBr layer at 0.1 C. f) Voltage profiles of LFP/Li ASSLB with Li<sub>2</sub>OHBr layer at different rates. All the above measurements were conducted on the battery tester at 80 °C.

tested, and the specific capacity remains  $124.5 \text{ mAh g}^{-1}$  at 21<sup>th</sup> cycle after switching the rate from 0.5 C to 0.05 C (Figure 6c), which indicates that the LFP/Li ASSLB with Li<sub>2</sub>OHBr layer can withstand moderate rate tests. Overall, according to the above cycle performances of the LFP/Li ASSLBs, it can be concluded that the introduction of Li<sub>2</sub>OHBr layer in the interface between LAGP and Li metal can improve the cycling stability of LFP/Li ASSLBs from the perspective of Li metal anode protection. However, the discharge polarization is still inevitable after a long-term cycle of the ASSLBs due to the low ionic conductivity of the SSEs and the complex interface mechanism, pending further study and resolution.

### 3. Conclusions

In summary, taking the advantage of low melting point ( $\sim 258^\circ\text{C}$ ) of the antiperovskite Li<sub>2</sub>OHBr, the protective layer on the surface of LAGP pellet was formed by a simple method of rapid solidification of molten Li<sub>2</sub>OHBr, and the dense and smooth Li<sub>2</sub>OHBr layer was observed with SEM. The Li/Li symmetric cells with Li<sub>2</sub>OHBr protective layer exhibit long-term cycle stability, compared with those using bare LAGP pellet. XPS analysis revealed the possible mechanism of the reaction between LAGP and Li metal, that is, Ge<sup>4+</sup> is reduced to Ge<sup>3+</sup> and Ge metal. Also, the stability of Li<sub>2</sub>OHBr-protected LAGP against Li metal was verified by XPS analysis, which suggests that the ionic conductivity and electronic insulation of Li<sub>2</sub>OHBr layer between LAGP and Li metal not only facilitate the shuttle of Li-ions, but also can effectively avoid the reduction of LAGP by Li metal. Furthermore, the assembled LFP/Li ASSLBs with Li<sub>2</sub>OHBr layer remained the specific capacity of  $96.3 \text{ mAh g}^{-1}$  after 40<sup>th</sup> cycle at 0.1 C and  $124.5 \text{ mAh g}^{-1}$  at 21<sup>th</sup> cycle after switching the rate from 0.5 C to 0.05 C. This work shows that LiRAP Li<sub>2</sub>OHBr possesses a considerable effect on Li-metal anode protection, and offers a straightforward strategy to protect SSEs that are unstable against Li metal.

## Experimental Section

### Preparation of Li<sub>2</sub>OHBr-protected LAGP Pellet

The LAGP pellets were prepared by pressing the commercial LAGP powder (mean particle size: 0.3  $\mu\text{m}$ ; purity: 99.9%) in the mold and sintering at  $950^\circ\text{C}$  for 10 h. The LiRAP-Li<sub>2</sub>OHBr was prepared by simply grinding stoichiometric amounts of LiOH (> 99%) and LiBr (> 99%) and one-step sintering at  $300^\circ\text{C}$  for 1 h. Interestingly, it has been recently reported that Li<sub>2</sub>OHBr was prepared by ball milling at room temperature, which indicates that the LiRAP family has a significant advantage in preparation compared to other electrolytes such as garnet-type and perovskite-type (more than  $1000^\circ\text{C}$ ). Then, the prepared Li<sub>2</sub>OHBr was heated to molten-state in a nickel crucible, and the sintered LAGP pellet was put into the molten liquid of Li<sub>2</sub>OHBr and clamped out with tweezers (Figure 1S). Naturally, the Li<sub>2</sub>OHBr-protected LAGP pellet was formed with the rapid solidification of molten-Li<sub>2</sub>OHBr on LAGP surface at room temperature. Further, the Li<sub>2</sub>OHBr-protected LAGP pellet was annealed at  $240^\circ\text{C}$  for 10 h to densify the Li<sub>2</sub>OHBr layer and

optimize the interface between Li<sub>2</sub>OHBr and LAGP. All the above preparations were performed under Ar atmosphere.

### Material Characterizations

X-ray diffraction (XRD) measurements were conducted on a Rigaku SmartLab 9 kW diffractometer with Cu K $\alpha$ 1 radiation ( $\lambda = 1.5406 \text{ \AA}$ ) to identify the phase of the powder and pellet samples. Before measurements, the Li<sub>2</sub>OHBr powder and Li<sub>2</sub>OHBr-protected LAGP pellet were sealed with Kapton film under the inert atmosphere for the hygroscopicity of LiRAP. Differential Scanning Calorimetry (DSC) analysis was conducted on a NETZSCH STA 449 instrument, and samples were sealed in aluminum crucible under N<sub>2</sub> atmosphere with a heating and cooling rate of  $5^\circ\text{C}/\text{min}$  from 30 to  $280^\circ\text{C}$ . The field emission scanning electron microscopy (SEM, Hitachi SU8230) was used to observe the surface and cross-sectional morphology of the solid electrolyte. The stability of the interface between SSEs and Li metal was analyzed by the X-ray photoelectron spectroscopy (XPS, PHI 5000 VersaProbe II) with Al K $\alpha$  X-rays. All the preparations of samples and measurements were performed under Ar atmosphere.

### Electrode Preparation and Cell Assembly

The cathodes for the ASSLBs were prepared by mixing the commercial LiFePO<sub>4</sub> (LFP), super P, PVDF, and LITFSI (60:12:20:8 by weight) in NMP to form a uniform slurry. Then the slurry was cast on a carbon-coated aluminum foil to produce an electrode film with an active material loading of around  $1.29 \text{ mg/cm}^2$ , which was dried at  $80^\circ\text{C}$  for 12 h under Ar atmosphere. The cathode films were cut into 10 mm diameter discs, and 2032 coin-type cells were fabricated in an Ar-filled glove box with Li foil as the anode. It should be noted that the composite membrane (CM) was introduced in the interface to realize intimate interfacial contact between cathode and SSEs, which was prepared by mixing the ZIF-67, PEO, and LITFSI (4:8:1 by weight) in Acetonitrile and casting on the side (no Li<sub>2</sub>OHBr layer) of the SSEs with enough drying time ( $\sim 12$  h) at  $60^\circ\text{C}$ . Here, ZIF-67 was chosen as the component of the composite membrane in order to increase the mobility of PEO chains, and ZIF-67 possesses a high surface area, rich porosity, and uniform channels, which can effectively benefit the Li<sup>+</sup> plating/stripping between the interface.<sup>[27]</sup>

### Electrochemical Measurements

Ionic conductivities were obtained from electrochemical impedance spectroscopy (EIS) in the temperature range of  $25\text{--}100^\circ\text{C}$ , using an electrochemical workstation analyzer (AUTOLAB M204) at frequencies ranging from 1 Hz to 1 MHz. During the EIS measurements, both sides of the sintered LAGP pellets were coated with sputtered Au films as the current collectors. Li<sub>2</sub>OHBr powders were hot-pressed into pellets (diameter = 10 mm) in an insulative die with an annealing temperature of  $120^\circ\text{C}$  for 10 h, and two stainless-steel rods were clamped on both sides of Li<sub>2</sub>OHBr as the current collectors. Galvanostatic cycling of symmetric batteries (Li/Li<sub>2</sub>OHBr-LAGP/Li) were sealed in 2032 coin-type cells and carried out at different current densities (0.05, 0.10, 0.15, 0.20 mA/cm<sup>2</sup>) after heating at  $130^\circ\text{C}$  for 10 h. When testing the impedance of Li/Li symmetric cells, the battery tester will be automatically suspended at the time set by the computer program, and the cells were always placed in an  $80^\circ\text{C}$  oven during the measurement. Galvanostatic charge-discharge cycling of all-solid-state LiFePO<sub>4</sub>/Li batteries was carried out between 2.7 and 3.9 V at a rate of 0.1 C. For the rate performance, ASSLBs were tested at different rates of 0.05, 0.1, 0.2, and 0.5 C. All the above measurements were

conducted on the Wuhan Land battery tester at 80 °C, and all cells were laid aside at this temperature for 6 h before testing.

## Acknowledgments

This work was financially supported by the Key Program of the National Natural Science Foundation of China (51732005), National Natural Science Foundation of China (51825201), Guangdong Provincial Key Laboratory of Energy Materials for Electric Power (2018B030322001), Shenzhen Key Laboratory of Solid State Batteries (ZDSYS20180208184346531), Key Laboratory of Energy Conversion and Storage Technologies (Southern University of Science and Technology), 21 C Innovation Laboratory of Contemporary Amperex Technology Ltd (21 C-OP-202009).

## Conflict of Interest

The authors declare no conflict of interest.

**Keywords:** solid-state electrolytes • all-solid-state lithium batteries • antiperovskite • NASICON • interface

- [1] a) B. Dunn, H. Kamath, J.-M. Tarascon, *Science* **2011**, *334*, 928; b) L. Lu, X. Han, J. Li, J. Hua, M. Ouyang, *J. Power Sources* **2013**, *226*, 272–288.
- [2] P. Jaumaux, J. Wu, D. Shanmukaraj, Y. Wang, D. Zhou, B. Sun, F. Kang, B. Li, M. Armand, G. Wang, *Adv. Funct. Mater.* **2021**, *31*, 2008644.
- [3] K. Park, J. B. Goodenough, *Adv. Energy Mater.* **2017**, *7*, 1700732.
- [4] D. Aurbach, E. Zinigrad, Y. Cohen, H. Teller, *Solid State Ionics* **2002**, *148*, 405–416.
- [5] L. Fan, S. Wei, S. Li, Q. Li, Y. Lu, *Adv. Energy Mater.* **2018**, *8*, 1702657.
- [6] a) T. K. Schwietert, V. A. Arszelewski, C. Wang, C. Yu, A. Vasileiadis, N. J. J. de Klerk, J. Hageman, T. Hupfer, I. Kerkamm, Y. Xu, E. van der Maas, E. M. Kelder, S. Ganapathy, M. Wagemaker, *Nat. Mater.* **2020**, *19*, 428–435; b) Z. Gao, H. Sun, L. Fu, F. Ye, Y. Zhang, W. Luo, Y. Huang, *Adv. Mater.* **2018**, *30*, 1705702.
- [7] E. Quartarone, P. Mustarelli, *Chem. Soc. Rev.* **2011**, *40*, 2525–2540.
- [8] V. Thangadurai, S. Narayanan, D. Pinzarlu, *Chem. Soc. Rev.* **2014**, *43*, 4714–4727.
- [9] a) J. C. Bachman, S. Muy, A. Grimaud, H.-H. Chang, N. Pour, S. F. Lux, O. Paschos, F. Maglia, S. Lupart, P. Lamp, L. Giordano, Y. Shao-Horn, *Chem. Rev.* **2016**, *116*, 140–162; b) M. Zhang, Z. Huang, J. Cheng, O. Yamamoto, N. Imanishi, B. Chi, J. Pu, J. Li, *J. Alloys Compd.* **2014**, *590*, 147–152.
- [10] a) P. Hartmann, T. Leichtweiss, M. R. Busche, M. Schneider, M. Reich, J. Sann, P. Adelhelm, J. Janek, *J. Phys. Chem. C* **2013**, *117*, 21064–21074;
- b) M. Hou, F. Liang, K. Chen, Y. Dai, D. Xue, *Nanotechnology* **2020**, *31*, 132003; c) Y. Liu, Q. Sun, Y. Zhao, B. Wang, P. Kaghazchi, K. R. Adair, R. Li, C. Zhang, J. Liu, L. Y. Kuo, Y. Hu, T. K. Sham, L. Zhang, R. Yang, S. Lu, X. Song, X. Sun, *Appl. Mater. Interf.* **2018**, *10*, 31240–31248.
- [11] a) H. Chung, B. Kang, *Chem. Mater.* **2017**, *29*, 8611–8619; b) J. Tippens, J. C. Miers, A. Afshar, J. A. Lewis, F. J. Q. Cortes, H. Qiao, T. S. Marchese, C. V. Di Leo, C. Saldana, M. T. McDowell, *ACS Energy Lett.* **2019**, *4*, 1475–1483; c) Y. Liu, C. Li, B. Li, H. Song, Z. Cheng, M. Chen, P. He, H. Zhou, *Adv. Energy Mater.* **2018**, *8*.
- [12] a) Q. Cheng, A. Li, N. Li, S. Li, A. Zangiabadi, T.-D. Li, W. Huang, A. C. Li, T. Jin, Q. Song, W. Xu, N. Ni, H. Zhai, M. Dontigny, K. Zaghib, X. Chuan, D. Su, K. Yan, Y. Yang, *Joule* **2019**, *3*, 1510–1522; b) Z. Zhang, Y. Zhao, S. Chen, D. Xie, X. Yao, P. Cui, X. Xu, *J. Mater. Chem. A* **2017**, *5*, 16984–16993.
- [13] J. A. Lewis, F. J. Q. Cortes, M. G. Boebinger, J. Tippens, T. S. Marchese, N. Kondekar, X. Liu, M. Chi, M. T. McDowell, *ACS Energy Lett.* **2019**, *4*, 591–599.
- [14] a) Z. Zhang, S. Chen, J. Yang, G. Liu, X. Yao, P. Cui, X. Xu, *Electrochim. Acta* **2019**, *297*, 281–287; b) G. Hou, X. Ma, Q. Sun, Q. Ai, X. Xu, L. Chen, D. Li, J. Chen, H. Zhong, Y. Li, Z. Xu, P. Si, J. Feng, L. Zhang, F. Ding, L. Ci, *Appl. Mater. Interf.* **2018**, *10*, 18610–18618.
- [15] D. Bosababu, J. Sivaraj, R. Sampathkumar, K. Ramesha, *ACS Appl. Mater. Interfaces* **2019**, *2*, 4118–4125.
- [16] a) Y. Wang, H. Zhang, J. Zhu, X. Lü, S. Li, R. Zou, Y. Zhao, *Adv. Mater.* **2020**, *32*, 1905007; b) Y. Zhao, L. L. Daemen, *J. Am. Chem. Soc.* **2012**, *134*, 15042–15047.
- [17] Y. Meesala, C.-Y. Chen, A. Jena, Y.-K. Liao, S.-F. Hu, H. Chang, R.-S. Liu, *J. Phys. Chem. C* **2018**, *122*, 14383–14389.
- [18] Z. D. Hood, H. Wang, A. Samuthira Pandian, J. K. Keum, C. Liang, *J. Am. Chem. Soc.* **2016**, *138*, 1768–1771.
- [19] L. Yin, H. Yuan, L. Kong, Z. Lu, Y. Zhao, *Chem. Commun.* **2020**, *56*, 1251–1254.
- [20] Y. Li, W. Zhou, S. Xin, S. Li, J. Zhu, X. Lu, Z. Cui, Q. Jia, J. Zhou, Y. Zhao, J. B. Goodenough, *Angew. Chem. Int. Ed. Engl.* **2016**, *55*, 9965–9968.
- [21] M. K. Sugumar, T. Yamamoto, M. Motoyama, Y. Iriyama, *Solid State Ionics* **2020**, *349*, 115298.
- [22] T. Famprakis, P. Canepa, J. A. Dawson, M. S. Islam, C. Masquelier, *Nat. Mater.* **2019**, *18*, 1278–1291.
- [23] a) D. Y. Oh, Y. E. Choi, D. H. Kim, Y.-G. Lee, B.-S. Kim, J. Park, H. Sohn, Y. S. Jung, *J. Mater. Chem. A* **2016**, *4*, 10329–10335; b) Z. Zhang, S. Chen, J. Yang, J. Wang, L. Yao, X. Yao, P. Cui, X. Xu, *Appl. Mater. Interf.* **2018**, *10*, 2556–2565; c) X. Yao, N. Huang, F. Han, Q. Zhang, H. Wan, J. P. Mwizerwa, C. Wang, X. Xu, *Adv. Energy Mater.* **2017**, *7*, 1602923.
- [24] Y. Zhao, Z. Huang, S. Chen, B. Chen, J. Yang, Q. Zhang, F. Ding, Y. Chen, X. Xu, *Solid State Ionics* **2016**, *295*, 65–71.
- [25] M. Weiss, D. A. Weber, A. Senyshyn, J. Janek, W. G. Zeier, *ACS Appl. Mater. Interfaces* **2018**, *10*, 10935–10944.
- [26] Á. RéVÉSz, *J. Mater. Sci.* **2005**, *40*, 1643–1646.
- [27] R. Zhao, Y. Wu, Z. Liang, L. Gao, W. Xia, Y. Zhao, R. Zou, *Energy Environ. Sci.* **2020**, *13*, 2386–2403.

Manuscript received: May 30, 2021

Accepted manuscript online: June 1, 2021

Version of record online: July 9, 2021